Int. j. adv. multidisc. res. stud. 2023; 3(2):773-780

Received: 16-02-2023
Accepted: 26-03-2023

International Journal of Advanced Multidisciplinary Research and Studies

ISSN: 2583-049X

Effect of Temperature on Biomechanical Properties of Carbonated Hydroxyapatite Bioceramics for Bone and Tissue Engineering Applications

[1] Iliya Ezekiel, [2] Amoko Oluwole

[1, 2] Department of Ceramic Technology, School of Applied Science and Technology, Federal Polytechnic Auchi State, Nigeria

Corresponding Author: **Iliya Ezekiel**

Abstract

Nowadays bioceramics are finding increasing applications in bone and tissue engineering due to their ability to stimulate remineralisation. Carbonated hydroxyapatite bioceramics was prepared using a one-step chemical wet co-precipitation method and sintered at 750, 800 and 850 °C respectively. Large part of the reacting starting materials of biogenic $CaCO_3$ powder was sourced from eggshell and then phosphatised at 80 °C for 6 Hrs. Temperatures effect on the microstructure and biomechanical features were examined with materials characterization tools: X-ray diffractometer (XRD), X-ray fluorescence (XRF), Transmission Electron Microscope (TEM), Field Emission Scanning Electron Microscopy (FE-SEM), Energy Disperse X-Ray Spectroscopy (EDS) and Induction Couple Plasma Optical Electronic Spectroscopy. In addition, the tensile strength, hardness and *in vitro* bioactivity will be analysed using Diametral Tensile Strength (DTS), Vickers hardness (H_v) and SBF media. ASTM C830 protocol was used to evaluate bulk density, water absorption, relative density and apparent porosity. The result showed enhanced mechanical properties (DTS: 1.59±0.18 - 6.52±0.28 MPa, H_v: 0.25±0.02 - 0.81±0.17 GPa) similar to the human cancellous bone and favourable bioactivity due to retention of acceptable carbonate content of 3.64 wt. % post-sintering.

Keywords: Carbonated Hydroxyapatite, Biomechanical, Bone and Tissue Engineering

1. Introduction

Broad studies have been committed to biomaterials in bone grafting substitute (BGS) as an alternative to autologous bone grafts for diseased/damaged bone treatment. This consensus is connected to a number of selection factors like mechanical properties to support new bone formation, proper porosity to allow cell migration as well as nutrients exchange and cytocompatibility to stimulate the cell proliferation (Youness, Taha and Ibrahim, 2019) [29]. The association of biomaterials' bone bonding ability and bone growth stimulation to the formation of carbonated hydroxyapatite (CHAp) establishes the bioactivity of such BGS. This type of apatite is chemically and structurally very comparable to the inorganic mineral phase of the natural hard tissues (Lizzi, Villata, Attika, N., Jackson, Grosgogeata and Goutaudier. 2017) [14]. Among the categories of biomaterials developed as bone substitute are bioceramics, metals, polymers and composites.

The calcium phosphate (CaP) mainly HA has been applied greatly as BGS due to its outstanding biocompatibility, bioactivity and nontoxicity features. Notably, the synthetic CHAp bioceramics with easy living cells resorption and possession of higher solubility than stoichiometric HA devoid of carbonate ions. The presence of CO_3^{2-}ions into the hexagonal structure of HA has been shown to enhance the mechanical properties of the bioceramics (Safarzadeh, Ramesha, Tan, Hari Chandran, Chinga, Ahmad-Fauzi, Krishnasamy and Ten, 2019) [21]. CaP allogenic materials display comparatively poor tensile and shear properties. Practically, the strength of the CaP ceramics is lesser than that of human hard tissue and, along their intrinsic brittleness, limits their usage to non-load bearing defects. Sintered calcium phosphate bioceramics have been revealed to possess improve mechanical properties due to thermal treatment at elevated temperatures. Biomechanical properties of biomaterials allows the materials to endure applied loads and displacements while retaining it biological reliability. The collective biomechanical properties of biomaterial include biocompatibility, biodegradability, bioactive, bio-functionality young modulus, strength, hardness, ductility and toughness (Siwar, Jamel and Ayed, 2013) [22].

Tissue engineering has been documented as one of the most effective procedure to substitute or repair damaged soft tissue and hard tissue such as the bone. The development of artificial regeneration of tissue is achieved by both *in vivo* and *in vitro* methods (Reddy and Reddy, 2018) [19]. Most times, the natural bone usually is fractured entirely or in part from trauma due to sport, fall or vehicular accident. In elderly individuals, pathologies such as osteoporosis may produce thinning of the bone causing the bone to be prone to fracture. The capacity to create bone-like materials with regenerative purposes for the

treatment of damaged or diseased bone during the course of humanity history was absent until the discoveries of third generation biomaterials. The introduction of third-generation biomaterials over the past decades such as metals, polymers, bioglasses, calcium carbonates and calcium phosphates (CaPs) became the game changer (Valley, 2017) [24]. CaP materials are conventional biomaterials for the augmentation of bone defects. They are obtainable as allogenic, sintered materials. CaP have been applied clinically to restore bone defects for many years. They can be categorised as hydroxyapatite ($Ca_{10}(PO_4)_6(OH)_2$, HA), fluorapatite ($Ca_{10}(PO_4)_6F_2$, FA), tricalcium phosphate ($Ca_3(PO_4)_2$, TCP), TCP-HA composites and TCP-FA composites that are used for medical and dental applications. CaP-based biomaterials and bioceramics are now employed in a numerous of diverse applications throughout the body, encompassing every parts of the skeleton. Applications include dental grafts, percutaneous devices and treatment of periodontal, remediation of bone defects, fracture treatment, whole joint replacement, orthopedics, cranio-maxillofacial reconstruction, otolaryngology and spinal surgery. CaP bioceramics among other biomaterials find applications in the development of both 2D and 3D scaffold structures for tissue engineering in *in vivo* and *in vitro* methods. Such approaches requires scaffolds that support the attachment, growth and proliferation of cells (Siwar *et al*., 2013) [22].

Traumatic injury is at the top position as a primary source of global mortality and disability across all spectrum. Projection by the World Health Organization (WHO) shows that the number of people living to octogenarian and older will increase globally by approximately 400 % in the next four decades. Hence, the number of old people suffering from severe health issues such as osteoporosis bone disease and bone fracture from low energy trauma will rise. Thus, a major effort such as develop diagnosis and medications, various fracture prevention strategies, and research, has been undertaken to curb and deal with already fracture/ diseased bone. Amid such research employed in the treatment of damaged and diseased bone in recent time is the use of CHA. Therefore, the aim of this research is to develop sintered carbonated hydroxyapatite bioceramics bone graft substitute. Also, to ascertain the effect of thermal treatment (750, 800 and 850 °C) on the biological features of the carbonated hydroxyapatite such as bioactivity using ion release study and simulated body fluid. The effect of variant temperatures on the mechanical properties of the carbonated hydroxyapatite like tensile strength and hardness would be comprehensively examined.

2. Materials and Methods

2.1 Materials synthesis

CHAp powder was prepared by a one-step co-precipitation method in agreement with the chemical equation Eq. 1.0:

$$10CaCO_3 + 6H_3PO_4 \rightarrow Ca_{10}(PO_4)_6(CO_3)_6(OH)_2 + 5H_2O + 1.5CH_4 + 2.5CO_2 \quad (1)$$

Calcium carbonate ($CaCO_3$) obtained from calcined eggshells and laboratory grade (H_3PO_4) were selected as sources of Ca^{2+} and PO_4^{3-}, respectively. Other important solvents used include sodium hydroxide (NaOH) and deionised water (H_2O). Deionised water serves as dissolution solvents and NaOH acts as pH regulator. The solid mass obtained from co-precipitation of the reactants at 80 °C for 6 Hrs. is then dried at 100 °C for 24 Hrs in an oven. The synthesized powder was pressed into pellets and sintered in a muffle furnace at 750, 800 and 850 °C, respectively. The sintered CHAp samples were designated with the following acronym C75 for 750 °C, C80 for 800 °C and C85 for 850 °C.

2.2 Characterization

The materials characterization will involve the use of X-ray diffractometry (XRD), X-ray fluorescence (XRF), Transmission Electron Microscope (TEM), Field Emission Scanning Electron Microscopy (FE-SEM), Energy Disperse X-Ray Spectroscopy (EDS) for investigating crystallinity, chemical constituent, particle sizes and morphology. The mechanical properties involving strength and relative density were measured using DTS, H_v and Archimedes apparatus set-up. In addition, simulated body fluid (SBF) and ion release studies were deployed to evaluate the bioactivity of the sintered samples C75, C80 and C85.

2.2.1 X-Ray Diffraction (XRD)

XRD in the interval of angles $20° \leq (2\theta) \leq 60°$ (Cu Kα radiation; Bruker Advanced X-ray Solution D8, Bremen, Germany) was used to determine the lattice parameter, crystallite size, and phase of powders. The X'Pert HighScore Plus software was used. Inferred patterns were matched with the International Center for Diffraction Data with file number 00-009-0432 designated for standard HA to estimate the phase type and size of crystals. The crystallite size was calculated by XRD through Scherrer's equation (Eq. (2.0)) (Wagoner Johnson and Herschler, 2011) [25]:

$$D_{scherrer} = \frac{K\lambda}{\beta \frac{1}{2} Cos\theta} \quad (2)$$

where D refers to the crystallite size (nm), λ (1.5404 Á) refers to the wavelength of Cu Kα radiate on, β) refers to the full width at half maximum (radian), θ is the diffraction angle (degrees), and k is the boarding constant (0.94). In this regard, distinct diffraction peaks of (002), (211), and (300) with high intensities, were selected for evaluation. Rietveld refinement was conducted on the chemical compound to confirm the effect of ions on the apatite structure.

2.2.2 X-Ray Fluorescence (XRF)

Emission of specific atomic energies of different elements permits an XRF spectrometer to analyze which elements are present in any given composition; the number of energies detected supply quantitative information (West, 2013) [26]. In this study, powders of each the CHAp samples were mixed each with a flux in a platinum crucible, heated to 1050 ˚C to form a glass bead. The various glass beads were used to quantify the atomic concentration of elements of various samples by XRF spectrometer (Rix 3000; Rigaku, Tokyo, Japan).

2.2.3 Fourier Transform Infra-Red (FTIR) Spectroscopy

In order to investigate the molecular vibrations by matching the unique infrared wave bands of a functional group with the vibrations of the functional groups, Infrared spectroscopy was deployed. Two kinds of vibrations in the mid-infrared region (4,000 – 1,000 cm^{-1}): (i) the stretching vibrations (*v*), affect bond-length changes and (ii) the

bending vibrations (δ-in plane, π-out of plane) influence changes in bond angles (Berthomieu and Hienerwadel, 2009) [5].

The types of bonding and chemical distinctiveness were determined by FTIR (Spectrum 1; Perkin-Elmer, Waltham, MA, USA) in the 400 – 4000 cm^{-1} range with the help of the Spectrum software. 0.4 to 1.0 mg of each the CHAp composition was mixed with 200 to 400 mg of KBr manually milled and pressed with a force of 28 MPa for 2 minutes into a translucent wafer. Finally, the compact pellet was transferred into the machine and then probed in a transmittance mode.

2.2.4 Field Emission Scanning Electron Microscopy (FE-SEM)

FE-SEM operation was achieved by the liberation and acceleration of high-energy beam of electrons in a raster scan pattern from field emission gun sources. In this study, the morphology of the sintered pellet surfaces of C75, C80 and C85 were examined by FE-SEM (S35VP; Zeiss, Dublin, CA, USA). In addition, the formation of apatite layer on all sintered pellets immersed in SBF solution were analyzed using FE-SEM. The samples were prepared by sputtering of gold film on samples to form a surface coat. The surface coat ensured effective surface conductivity of the samples that prevents image defects.

2.2.5 Energy Disperse X-Ray Spectroscopy (EDS)

Assembled with the FE-SEM, the EDS was employed in ascertaining the elemental composition based on a spot or area of a sample. The system consist of three basic components that are made to work together to achieve optimum results: they include the X-ray detector or spectrometer, the pulse processor, and the analyzer (Pool, 2013) [18]. The EDS is designed to detect all elements with atomic number range between Be-4 to U-92, however the non-detection of light-elements (Z < 10) are due to limitation of certain instrument design (E. and M., 2013). The C C80 pellets surfaces were prepared to be electrically conducting to facilitate transmittance of electron on the samples incident surface. The vacuum evaporates sputtered surface coat which is applicable to FE-SEM should be about 10 nm in thickness. The appropriate sputtered thickness is necessary to avoid peak intensity and charging phenomenon.

2.3 Mechanical Testing

2.3.1 Density, water absorption and porosity of the sintered pellets

The apparent or bulk density, water absorption and porosity of the C75, C80 and C85 pellets were evaluated in accordance with Standard Archimedes technique established by ASTM C830-00. This protocol (ASTM C830-00) covers standard test methods for calculating apparent porosity, liquid absorption, apparent specific gravity and apparent or bulk density of refractory shape specimen using vacuum pressure. In this work, possible moisture content in C75, C80 and C85 pellets were eliminated by heating at 100 ˚C for 2 hours prior to density measurement. Then, the moisture-free sintered pellets dry weight (D) was recorded. To obtain properly soaked pellets, the samples were placed into beakers containing deionized water and vacuum for 1 hour. Thereafter, Sartorius® balance and bulk density apparatus recorded the saturated weight (W) and suspended weight (S).

The pellets were transferred on a damped cotton surface after vacuuming to eliminate surface water and precaution was taken not over damp as this may induce false reading during weighing. The pellet was then transferred from the damped surface onto the upper pan platform where the saturated weigh (W) was recorded. Immediately, measured W pellet moved down to the weigh basket submerged under the water and the suspended weight (S) was observed. From this procedure, bulk density, relative density, water absorption and apparent porosity were estimated using Eq. 3.0, 4.0 and 5.0:

$$\text{Bulk density } (gcm^{-1}): \rho_{bulk} = \frac{D}{W-S} \quad (3)$$

$$\text{Relative density, RD } (\%): = \frac{\rho_{bulk}}{D_{CHA}} \times 100 \quad (4)$$

$$\text{Apparent porosity, AP } (\%): = \frac{W-D}{W-S} \times 100 \quad (5)$$

D_{CHA} is the theoretical density of each specific sample, which is represented in the Eq. 6.0 (Alshemary *et al*., 2018):

$$D_{CHA}\,(gcm^{-1}) = \frac{ZM}{A_n V} \quad (6)$$

where Z is the number of molecules per unit cell, M is the molecular weight of the sample, A_n is the Avogadro's number (6.022×10^{23}) and V ($3^{½}/a^2.c$) is volume unit cell from XRD data.

2.3.2 Diametral Tensile Strength (DTS) and Hardness (H_v)

The Instron 3369 universal test model device was used in this study to evaluate the DTS values for the C75, C80 and C85 pellets. The pellets were placed vertically on the lower platform in between two stainless steel plates and a compressive load mode is applied at a rate of 0.5 mm $min.^{-1}$. Upon fracture, the DTS value is calculated as the tensile stress in the x-direction in the disc (pellet) diameter given by x = 0, z = 0, assuming plane stress and a point load in accordance with Eq. 7.0 (Perez-Gonzalez *et al*., 2011) [17]:

$$\text{DTS (MPa)} = \frac{2P}{\pi D t} \quad (7)$$

where p is the applied load (Nmm^2), D is the diameter of pellet (mm), t is the thickness of the pellet (mm) and π is the pie constant, 3.14.

In this study, the samples were first ground on wet SiC abrasive papers with the various ANSI: American National Standards Institute grit sizes of 240, 320, 400, 600 and 800 (1 ANSI = 1.29 µm). Thereafter, the ground samples were polished with liquid alumina of fine particle sizes of 1.0, 0.3 and 0.05 µm. Precaution was taken during polishing by anti-clock wise and occasionally '*8*' shape movement to ensure uniformly flat surface. Then, the vickers hardness measurements were performed in air at room temperature under a constant loading condition using a load of 3 kgf for a dwelling time of 10 s by Vickers Hardness Tester Mitutoyo HV-114. The hardness was measured five points on each pellet embedded in resin and polished to a submicron surface finish. Vickers hardness (H_v) was

calculated according to Eq. 8.0 (Alb *et al*., 2009) [1].

$$H_v = \frac{1.854P}{\left(d_1 + d_2/2\right)^2} \quad (8)$$

Where P is the applied load, d_1 and d_2 are the diagonal indent lengths in mm. H_v is unitless which can be converted to MPa by $H_v \times 9.807$ or to GPa by $H_v \times 0.09807$.

2.4 In vitro Bioactivity ad pH Profile

The C75, C80 and C85 pellets bioactivity study was conducted *in vitro* by using simulated body fluid (SBF) solution prepared in accordance with the procedure established by (Kokubo and Takadama, 2006) [11] and reviewed by ISO 23317 (Kolafova *et al*., 2017) [17]. The carbonated HA sintered pellets were assessed for apatite forming ability and ions release activities.

The volume of the SBF solution required for each sintered pellet was estimated by Eq. 9.0 (Kokubo and Takadama, 2006) [11].

$$V_s = S_a / 10 \quad (9)$$

wherein Vs is the volume of the SBF in mL and Sa is the apparent surface area of the specimen in mm^2.

The Sa was determined by the surface area of the cylindrical pellet shape by Eq. 10.0.

$$S_a = 2\pi r^2 + 2\pi h \quad (10)$$

where r is the radius and h the height or thickness in mm of the pellets.

An average V_s of ~30 mL the prepared SBF solution was poured into the calibrated plastic vial and the sintered pellet carefully submerged as shown in Fig. 3.10. Then, the vials are placed in a rack and transferred into a control oven with simulating body temperature for 7, 14, and 21 days. The pH was recorded at predetermined sessions and FESEM was employed to evaluate the apatite layer and morphology of the samples. Inductively Coupled Plasma Optical Emission Spectroscopy (ICP-OES) quantified the SBF ion released of Ca^{2+} and P^{5+}, in leachates.

The samples are introduced into the ICP-OES's plasma in a process that desolvates, ionises, and excites the same samples. Composition in the form the sample elements are assesed by their unique emission lines and measured intensity of the given lines. The leachate was converted into fine aerosol vapor, which allowed for transportation via a nebulizer with an argon stream into a plasmatic burner. The concentrations of the samples were measured at wavelengths of Ca^{2+}; 393.366 nm and P^{5+} 177.499 nm respectively.

3. Result and Discussion

3.1 Characterization

3.1.1 X-ray diffractometry (XRD)

The XRD profile showed that the crystal geometry of the apatite samples remained intact with all C75, C80 and C85 pellets after sintering at 750ºC, 800ºC and 850ºC respectively. Reference match with a standard in substituted HA may indication for structurally stable and favorable ionic incorporation of CO_3^{2-} (Swamiappan, 2016) [23]. In Fig. 1, the peaks correspond to reference HA ICDD: 009-0432 patterns and minor constituent of CaO phase. Generally, incorporation of CO_3^{2-} and CO_2 environment creates a poorly crystalline HA phase, which turns crystalline upon thermal treatment (Krajewski *et al*., 2005) [13]. The inclination towards a typical crystalline HA peaks with minor CaO peaks at around 2θ = 29.5º and 39.4º was observed for various sintering schedules. The presence of trace phase of CaO peaks was reported to be cause by reaction between CO_2 from partial decomposed CHAp and in situ Ca^{2+} (Garskaite *et al*., 2014) [7].

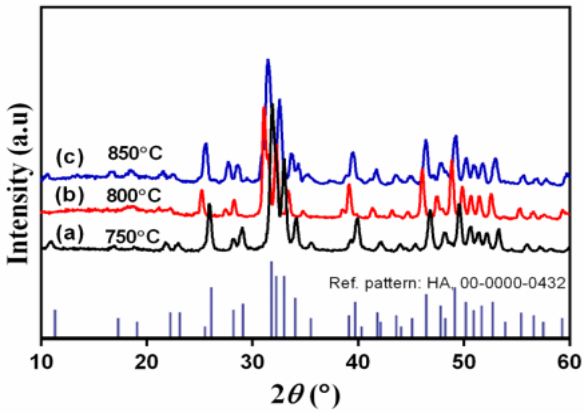

Fig 1: XRD of sintered pellets (a) C75 (b) C80 and (c) C85

In Fig. 1 (a), C75 showed a distinct peaks at 2θ /plane = 25.90º/ (002), 31.80º/ (211), 32.93º/ (300), 34.09º/ (202), 39.83º/ (310), 46.72º/ (222), 49.50º/ (213) and 53.21º/ (004) correspond to reference HA. At the sintering temperature of 750 ºC (Table 1) the C75 sample demonstrated a crystallite size ($d_{Scherer}$) of 28.7 nm and crystallinity percent (X_C%) of 81.08 nm. The increase in lattice strain associated with micro stress and dislocation was reported to affect diminution of crystals in apatite (Wopenka and Pasteris, 2005) [27].

Table 1: Crystal features of samples sintered at variant temperatures

Sample	Lattice constant			$d_{Scherer}$	Lattice (ε)	FWHM	X_C%
CHAp	*a* (Å)	*c* (Å)	*c*/*a*	(nm) [x]	(%) [y]	(º)	(%) [z]
C75	9.424	6.886	0.731	28.7	0.385	0.296	81.08
C80	9.417	6.879	0.730	34.68	0.330	0.245	97.96
C85	9.219	6.848	0.743	25.15	0.441	0.245	71.01

[X] Scherer calculator, [Y] Lattice strain, [Z] Crystallinity percent

Similarly, C80 in Fig. 1(b) revealed an analogous peaks to reference HA (ICDD: 009-0432) at 2θ/plane include, 25.79º/ (002), 31.64º/ (211), 32.78º/ (300), 33.93º/ (202), 39.68º/ (310), 46.58º/ (222), 49.36º/ (213) and 53.08º/ (004). Table 1 showed that at sintering temperature of 800ºC the crystallite size of 34.68 nm and crystallinity percent of and 97.96 %. Sample C85 at a relatively higher sintering temperature of 850 ºC in Fig. 1(c), a match with reference HA is observed at 2θ /plane = 25.64º/ (002), 32.03º/ (211), 33.28º/ (300), 34.12º/ (202), 40.35º/ (310), 47.15º/ (222), 49.70º/ (213) and 53.11º/ (004). It is interesting to note that C85 possessed the lowest diminutive particle as reflected in its crystallite size of 25.15 nm as well as high relatively lower crystallite percentage of 71.01 %.

3.1.2 X-Ray Fluorescence (XRF) and SEM-EDS

The evaluation of the sintered samples at variant temperature by XRF showed compositions after decomposition of volatile. EDS (Figure 2) was used to confirm the presence of Carbon at 800 ˚C which is none detectable by XRF due to lack compatible C-filters. In Table 2, the oxygen content of C75, and C80 were relatively the same (58.6496 and 58.3050 wt. %). However, C85 pellets revealed a steep oxygen expansion of 60.3160wt. % due to more evolution of volatile content associated with higher sintering temperature. Similarly, the relative lower Ca/P ratio of C85 in comparison to C75 and C80 can be attributed to the partial decomposition of CO_3^{2-} content at the PO_4^{3-} site at elevated temperature.

Table 2: Elemental composition of sintered pellets at different temperatures

Compositions (wt. %)					
CHAp	**Ca**	**P**	**O**	**C♣**	**Ca/P**
C75	27.2851	14.0653	58.6496	-	1.94
C80	27.4799	14.2151	58.3050	3.64	1.93
C85	24.7701	14.9193	60.3160	-	1.66

♣ Energy Disperse X-Ray Spectroscopy (EDS)

The result from the SEM-EDS in Fig. 2 further validate the result from XRF by area mapping confirmation of the presence of Ca, P and O in sintered pellet C80. Mapping involving area-detection of a sample as indicated in red rectangle outline offers a more precise result than point-detection. Elemental composition by weight found in EDS as compared to XRF was slighted higher: Ca^{2+} XRF/EDS 27.4799/35.54 wt. % and P^{5+} XRF/EDS 14.2151/20.05 wt. %. This difference was due to limited probing of bulk ions present in sample associated with EDS, which gives a less precisely higher reading. On the order hand, XRF guarantees bulk ion probing and a more reliable composition data.

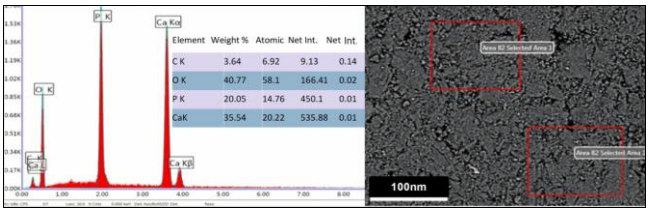

Fig 2: SEM-EDS of peaks and composition area mapped sintered pellets at 800 °C

3.1.3 Fourier Transformation Infrared (FTIR)

The FTIR analysis of the as synthesize sample and commercial HA is shown in Fig. 3. The results revealed consistent functional group bands associated with the as synthesized samples. However, narrow bands were common across all the functional group (PO_4^{3-}, $CO_3^{2-}$and OH^-) with the CO_3^{2-} bands showing a flattened modulation due to gradual loss of CO_2 at sintering temperatures. The band degenerations of the sintered samples were observed at 515cm^{-1} for v_4 PO_4^{3-}, 980cm^{-1} for v_1 PO_4^{3-} and 1082cm^{-1} for v_3 PO_4^{3-}, or asymmetrically P-O stretching vibration. The CO_3^{2-} bands were recorded at 879cm^{-1} for v_2 CO_3^{2-} or O-C-O bending vibration and 1430cm^{-1} for v_3 CO_3^{2-} or C-O stretching vibration. In Fig. 4.21, the various functional group of OH^- (1 and 2), CO_3^{2-} (3 and 5) and PO_4^{3-} (4 and 6) vibrations remain as B-type carbonated HA at a sintering temperature of 800 ˚C.

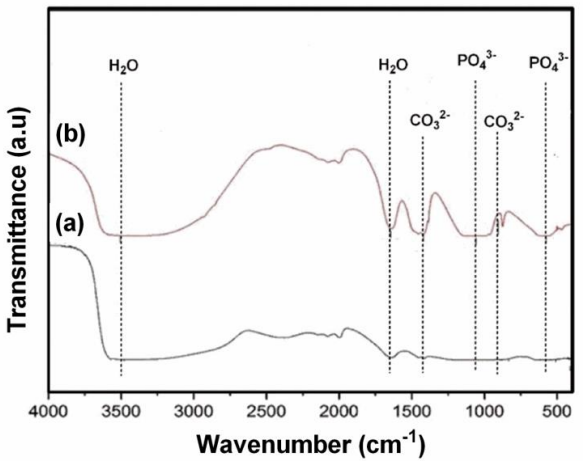

Fig 3: FTIR of (a) commercial HA (b) as synthesized CHAp powder

3.1.4 FE-SEM and Bioactivity of Sintered Pellets

The micrographs of the C75, C80 and C8 pellets sintered at various temperatures are shown in Fig. 4. The micrograph at 750 °C (Fig. 4 (a)) revealed a porous microsphere and self-assembly micrographs was established in a clear porous microsphere at 800 °C (Fig. 4(b)). The morphology at 850 °C in Fig. 4(c) showed a further consolidation of the porous microsphere. The shapes of the various morphology such as microsphere in this study is consistent with works reported on HA elsewhere (Sadat-Shojai *et al*., 2013) [20].

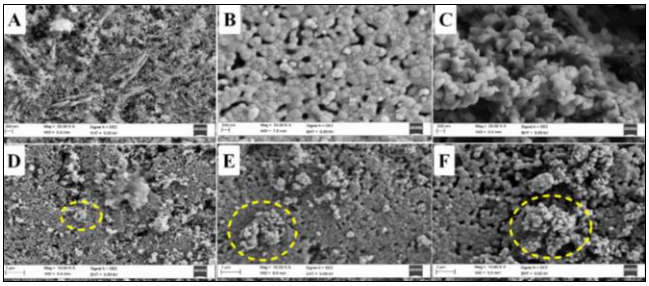

Fig 4: FE-SM Micrograph of sintered pellets (a) C75 (b) C80 (c) C85 and bioactivity after soaking in SBF solution (d) C75 day 7 (e) C80 day 7 (f) C85 day 7

Optimum sintered temperature of 800 ºC was selected for bioactivity and ion release study. The selection C80 for bioactivity study was due to a combination of stable CO^{3+} content, desired crystallinity for subsequent cell growth and cancellous bone-like strength. Temperatures exceeding 800 ºC favour the increase in DTS although deplete the carbonated content rapidly. The mechanism of apatite formation is largely dependent on interaction of the equal anionic-cationic component of SBF media with a negatively charged surface of HA. The SBF inherently composed of four anions (HCO_3^-, PO_4^{2-}, SO_4^{2-} and Cl^-) and four cations (Ca^{2+}, Mg^{2+}, Na^+ and K^+). A rich Ca^{2+}─ Ca^{2+} prevails on the surface of the pellet in the early stage of soaking which is then replaced by poor Ca^{2+}─ Ca^{2+}. Apatite crystals are formed at the pellets surface when poor Ca^{2+} and rich Ca^{2+} at surface of the pellets interact with PO_4^{2-} from the SBF solution (Kim *et al*., 2004) [10].

In this study, apatite layer formed in the control C75, C80 and C85 pellet (Fig. 4(d)-(f)) after soaking for 7 days in SBF solution displayed an early formation of apatite crystals. Larger non-dispersed flower-like apatite was evidently observed on all samples.

3.2 Mechanical Testing

Comprises of physical analysis such Bulk Density (BD), Relative Density (RD), Apparent Porosity, Water Absorption (WA) and strength test that consist of Diametral Tensile Strength (DTS) and Hardness (H_v).

Table 3: Physico-mechanical features of sintered pellets at different temperatures

		Physical				Strength	
	Temp.	***BD***	***RD***	***AP***	***WA***	**DTS**	**H_v**
Sample	**˚C**	**(g/cm)**	**(%)**	**(%)**	**(%)**	**(MPa)**	**(GPa)**
C75	750	1.36	43.1	50.00	26.86	1.59±0.18	0.25±0.02
C80	800	1.82	57.6	41.83	18.68	3.30±0.34	0.33±0.02
C85	850	2.13	67.5	29.24	12.06	6.52±0.28	0.81±0.17

The density of each sintered sample was measured five to six times by the Archimedes's principle using water as the fluid. The standard test method C830 ASTM (2006) is adopted in estimating density, water absorption and porosity. The bulk and relative density increases with increase in sintering temperature of C75, C80 and C85 as shown in Table 3. The reverse trend is observed for water absorption and open porosity as both quantities decrease with increase in temperature for all sintered samples. The maximum bulk density and a low water absorption (2.13 g/cm^3 and 12.06 %) were recorded C85. On the order hand, the minimum bulk density and an increased water absorption (1.36 g/cm^3 and 26.86 %) were noticed in C75.

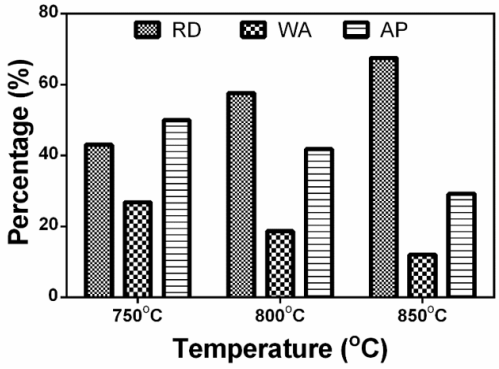

Fig 5: Relative density (RD), water and absorption (WA), apparent porosity (AP), (a) C75 at 750 °C, (b) C80 at 800 °C and (c) C85 at 850 °C

The thermal versus strength performance are shown in Table 3, Fig. 6 and Fig. 7. C85 with the least apparent porosity of 29.24 % exhibited a higher DTS and RD values of 6.52±0.28 MPa and 67.5 %. C80 revealed an average apparent porosity of 41.83 % revealed DTS and RD values of 3.30±0.34 MPa and 57.6 %. While C75 with a higher apparent porosity of 50.00 % revealed the least DTS and RD values of 1.59±0.18 MPa and 26.86 %.

In general, data from this study revealed that bulk pellet BD, DTS and RD increase while AP, and WA decrease with increasing sintering temperature. This trend was due to possibly sheer volume of constituent complete densification (Bang *et al.*, 2014) [4]. Previous study had suggested that higher sintering is needed to thermodynamically improve densification and kinetically relocated dopants to site (Dubnika and Zalite, 2014) [6].

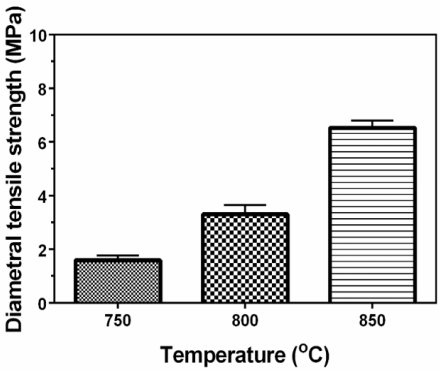

Fig 6: DTS of (a) C75 at 750 °C, (b) C80 at 800 °C and (c)C85 at 850 °C

In Table 3, the Vickers hardness value (H_v) increased with increase in temperature across each sample, however a deviation from the trend earlier established with DTS was noted. This was due to the procedural property associated to H_v as oppose to materials intrinsic property such as velocity, thermal conductivity, thermal diffusivity, emissivity etc. The procedural property justifies for the uncertainty of establishing traceability in hardness measurement (Hyung Tak *et al.*, 2013). Fig. 7 confirmed the overall lowest H_v value in C75 at 750 ˚C to be 0.25±0.02 GPa, a moderate C80 value of 0.33±0.02 GPa and the highest H_v in CHAII at 850 ˚C around 0.81±0.17 GPa. The mean Vickers hardness value (H_v) of cortical and cancellous bone has been reported to be 42/0.41 and 35 H_v/0.3432 GPa respectively (Ohman *et al.*, 2013) [16].

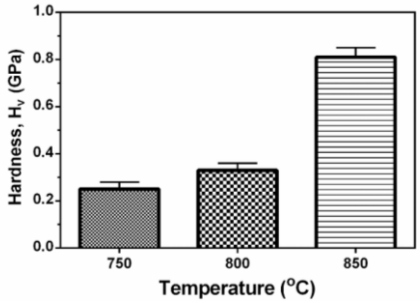

Fig 7: Hardness (H_v) of (a) C75 at 750 °C, (b) C80 at 800 °C and (c) C85 at 850 °C.

3.3 Ion release study and pH Profile

3.3.1 Calcium and phosphorus ion release

Ion release indicates the regulatory state in dissolution of CaP bioceramics due to the mobility of ions into the SBF solution or by occurring on the crystal surfaces. Therefore, the SBF medium hydrolyses ($Ca_2(HPO_4)(OH)_2$) as it becomes more acidic thus releasing more ions and hydrolyses less in an alkaline state (Hatim, 2015). The sintered C80 sample introduces surface irregularities and structural defects inside and on the surface bulk of CaP crystals. Thus, this creates dissolution nuclei that facilitate the rate of ion release. Fig. 8 indicated an increase in Ca^{2+} release after 7 days of immersion into SBF solution which then stabilized after 14 with a resurgence after 21 days. The high and resurgence Ca^{2+} between 7-21 days of soaking can

be attributed to higher participation of Ca^{2+} specie during soaking.

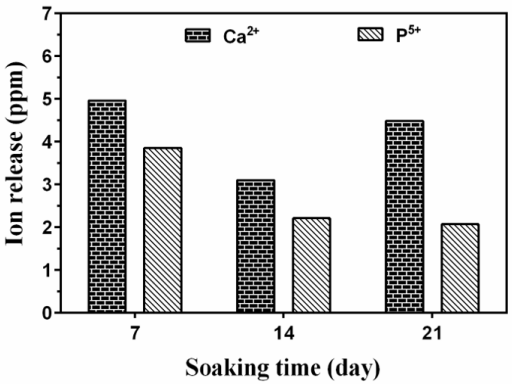

Fig 7: C80 ion release study of Ca^{2+} and P^{5+} at optimal temperature of 800 °C

In Fig. 7, the phosphorus release in all the samples increased until saturation after 14 days where it gradually stabilizes to day 21. The decrease trend of P ion release of C80 may signify the active participation of P in apatite formation was greater than dissolution rate (Xie *et al*., 2016).

3.3.2 pH Profile

The pH of SBF solution in the region of 7.4 (physiological environment) influence the dissolution and ion released mechanism that occur during soaking time. Thus, the fluctuation in pH of SBF has a direct correlation with the degradation kinetics of implants. In Fig. 8, the control C80 as the optimum sample was used and it showed stable neutral pH value neutral (~7.32) after day 7. The samples then slightly declined after day 14 (~7.28) and day 21 (~ 7.023). The reason for somewhat descend could be due cationic exchanges at the samples surface and the SBF solutions (Alshemary *et al*., 2016).

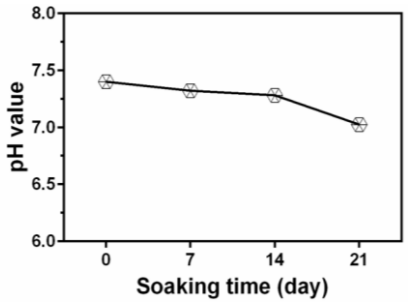

Fig 8: C80 pH profile optimal temperature of 800 °C

The stability of the pH media indicates a balance between dissolution/precipitation processes. The overall monitoring of the pH values showed healthy range of value within ~7.2-7.6 necessary for implant and body fluid interactions.

4. Conclusion

The results indicate higher mechanical feature for sintered C85 samples at 850 °C due to well define grain boundaries associated with higher temperature regime. The most bioactive sintered samples emanate from C80 pellet with a combination of robust porosity feature and carbonate content. The overall result from this research show that all samples can find application as bone graft substitute (BGS) for biomedical applications.

5. Conflict of Interests

The authors declare that there is no conflict of interests regarding the publication of this paper.

6. Acknowledgements

The authors would like to acknowledge the financial support of Tertiary Education Trust Fund (TETFund) and Auchi Polytechnic Auchi for the provision of conducive environment that brought about this research.

7. References

1. Alb C, Moldovan M, Prejmerean C, Trif S, Sarosi C, Dudea D, *et al*. Microstructure, mechanical properties and tissue/biomaterial interface behaviour of new dental restorative composites, 2009.
2. Alshemary AZ, Engin Pazarceviren A, Tezcaner A, Evis Z. $Fe^{(3+)}$ /$SeO_4^{(2-)}$ dual doped nano hydroxyapatite: A novel material for biomedical applications. J Biomed Mater Res B Appl Biomater. 2018; 106:340-352.
3. Alshemary AZ, Engin Pazarceviren A, Tezcaner A, Evis Z. Mesoporous Strontium Doped Nano Sized Sulphate Hydroxyapatite as Novel Biomaterial for Bone Tissue Applications, 2016.
4. Bang LT, Long BD, Othman R. Carbonate Hydroxyapatite and Silicon-Substituted Carbonate Hydroxyapatite: Synthesis, Mechanical Properties, and Solubility Evaluations. The Scientific World Journal, 2014, 969876.
5. Berthomieu C, Hienerwadel R. Fourier transform infrared (FTIR) spectroscopy. Photosynthesis Research. 2009; 101:157-170.
6. Dubnika A, Zalite V. Preparation and characterization of porous Ag doped hydroxyapatite bioceramic scaffolds. Ceramics International. 2014; 40:9923-9930.
7. Garskaite E, Gross KA, Yang SW, Yang TCK, Yang JC, Kareiva A. Effect of processing conditions on the crystallinity and structure of carbonated calcium hydroxyapatite (CHAp). CrystEngComm. 2014; 16:3950-3959.
8. Hatim Z. Effects of ions traces on the dissolution of bioceramics composed of hydroxyapatite and β-tricalcium phosphate, 2015.
9. Hyung Tak N, Moo Lee H, Gunwoong B. Effects of differences in hardness measurement procedures on the traceability chain and calibration process, 2013.
10. Kim HM, Himeno T, Kawashita M, Kokubo T, Nakamura T. The mechanism of biomineralization of bone-like apatite on synthetic hydroxyapatite: an *in vitro* assessment. Journal of The Royal Society Interface. 2004; 1:17-22.
11. Kokubo T, Takadama H. How useful is SBF in predicting *in vivo* bone bioactivity? Biomaterials. 2006; 27:2907-2915.
12. Kolafova M, Stovicek J, Strnad J, Zemek J, Dybal J. *In vitro* Bioactivity Test of Real Dental Implants According to ISO 23317. Int J Oral Maxillofac Implants. 2017; 32:1221-1230.
13. Krajewski A, Mazzocchi M, Buldini PL, Ravaglioli A, Tinti A, Taddei P, *et al*. Synthesis of carbonated hydroxyapatites: efficiency of the substitution and critical evaluation of analytical methods. Journal of Molecular Structure. 2005; 744-747:221-228.
14. Lizzi F, Villata C, Attika N, Jackson P, Grosgogeata B, Goutaudier C. Mechanical characteristic and biological

behaviour of implanted and restorative bioglasses used in medicine and dentistry: A systematic review. Dent Mater, 2017. Doi: 10.1016/j.dental.2017.03.017.
15. Obada DO, Dauda ET, Abifarin JK, Dodoo-Arhin D, Bansod ND. Mechanical properties of natural hydroxyapatite using low cold compaction pressure: Effect of sintering temperature, Materials Chemistry and Physics. 2020; 239:122099.
16. Ohman C, Zwierzak I, Baleani M, Viceconti M. Human bone hardness seems to depend on tissue type but not on anatomical site in the long bones of an old subject. Proc Inst Mech Eng H. 2013; 227:200-206.
17. Perez-Gonzalez A, Iserte-Vilar JL, Gonzalez-lluch C. Interpreting finite element results for brittle materials in endodontic restorations. Biomed Eng Online. 2011; 10:44.
18. Pool R. An Introduction to Energy-Dispersive and Wavelength - Dispersive X-Ray Microanalysis. Microscopy and Analysis. John Wiley & Sons Ltd, 2013.
19. Reddy R, Reddy N. Biomimetic approaches for tissue engineering, Journal of Biomaterials Science, Polymer Edition, 2018. DOI: 10.1080/09205063.
20. Sadat-Shojai M, Khorasani MT, Dinpanah-Khoshdargi E, Jamshidi A. Synthesis Methods for Nanosized Hydroxyapatite with Diverse Structures, 2013.
21. Safarzadeh M, Ramesh S, Tan CY, Chandran Y, Chinga YC, Ahmad-Fauzi MN, *et al*. Sintering behaviour of carbonated hydroxyapatite prepared at different carbonate and phosphate ratios, Bol. Soc. Esp. Cerám. Vidr, 2019. Doi: 10.1016/j.bsecv.2019.08. 001.
22. Siwar S, Jamel B, Ayed FB. Mechanical properties of biomaterials based on calcium phosphates and bioinert oxides for applications in biomedicine: Advances in Biomaterials Science and Biomedical Applications, 2013. Doi: 10.5772/53088.
23. Swamiappan S. Synthesis of carbonate substituted hydroxyapatite by Pechini method, 2016.
24. Valley C. Fractures and Trauma, 2017. Available: http://www.cvosm.com/fractures-and- trauma/ [Accessed 3rd January 2021].
25. Wagoner Johnson AJ, Herschler BA. A review of the mechanical behavior of CaP and CaP/polymer composites for applications in bone replacement and repair. Acta Biomaterialia. 2011; 7:16-30.
26. West M. X-ray fluorescence spectrometry and related techniques: An introduction. Momentum Press, 2013.
27. Wopenka B, Pasteris JD. A mineralogical perspective on the apatite in bone. Materials Science and Engineering: C. 2005; 25:131-143.
28. Xie L, Yu H, Yang W, Zhu Z, Yue L. Preparation, *in vitro* degradability, cytotoxicity, and *in vivo* biocompatibility of porous hydroxyapatite whisker-reinforced poly (L-lactide) biocomposite scaffolds. Journal of Biomaterials Science, Polymer Edition. 2016; 27:505-528.
29. Youness RA, Taha MA, Ibrahim M. *In vitro* bioactivity, molecular structure and mechanical properties of zirconia-carbonated hydroxyapatite nanobiocomposites sintered at different temperatures, Materials Chemistry and Physics, 2019. Doi: 10.1016/ j.matchemphys.2019.122011.